Northumbria Research Link

www.northumbria.ac.uk/nrl

northumbria
UNIVERSITY NEWCASTLE

Efficient spectral compression of wavelength-shifting soliton and its application in integratable all-optical quantization

Chao Mei[1], Jinhui Yuan[1,2,3,*], Senior Member, IEEE, Senior Member, OSA, Feng Li[2,3,*], Senior Member, OSA, Binbin Yan[1], Xinzhu Sang[1], Qiang Wu[4], Xian Zhou[2], Kuiru Wang[1], Chongxiu Yu[1], and Gerald Farrell[5]

[1]State Key Laboratory of Information Photonics and Optical Communications, Beijing University of Posts and Telecommunications, Beijing, P. R. China
[2]Photonics Research Centre, Department of Electronic and Information Engineering, The Hong Kong Polytechnic University, Hung Hom, Hong Kong S. A. R., P. R. China.
[3]The Hong Kong Polytechnic University Shenzhen Research Institute, Shenzhen, P. R. China.
[4]Department of Physics and Electrical Engineering, Northumbria University, Newcastle upon Tyne, NE1 8ST, United Kingdom.
[5]Photonics Research Centre, Dublin Institute of Technology, Dublin, Ireland.
*Corresponding authors: Jinhui Yuan; Feng Li (e-mails: yuanjinhui81@bupt.edu.cn; enlf@polyu.edu.hk)

Abstract: In this paper, we numerically demonstrate efficient spectral compression (SPC) of wavelength-shifting soliton in a chalcogenide strip waveguide. It is found that the profiles of group-velocity dispersion (GVD) and Kerr nonlinearity play key roles in determining SPC. After calculating the dispersion of Kerr nonlinearity and Raman spectrum for three kinds of chalcogenide materials, $Ge_{11.5}As_{24}Se_{64.5}$ is chosen as the material for designing the chalcogenide strip waveguide (CSW). The geometric parameters of CSW are optimized to obtain the desired GVD and Kerr nonlinearity. Simulation results show that in the designed CSW, an input spectrum width of 52.04 nm can be compressed to 7.23 nm along with wavelength shift of 17 nm when the input peak power is 25 W. With the input peak power increasing to 75 W, the SPC is slightly weakened, but wavelength shift can be up to 190 nm. The proposed CSW is applied to integrated all-optical quantization and an effective quantization number of 3.66-bit is achieved. It is expected that our research results can find important applications in on-chip integrated spectroscopy, all-optical signal processing, etc.

Index Terms: Raman solitons, spectral compression, all-optical quantization, chalcogenide strip waveguide.

1. Introduction

Robust, narrow-linewidth and wavelength-tunable light sources are very important for optical communication system, spectroscopy, and optical coherence tomography (OCT). At present, one of the effective methods to obtain such an optical source is spectral compression (SPC). SPC was firstly demonstrated in optical fibers in 1993 [1]. Self-phase modulation (SPM) can be used to achieve SPC in cascaded single-mode fiber and nonlinear medium [2]-[4], fibers with negatively chirped pulse [5, 6], photonic crystal fibers (PCFs) [7], [8] and dispersion-increasing fiber (DIF) [9]-[12]. However, SPC can only be realized within a narrowband range in these works, which limits its applications in OCT and multichannel communication. In 2010, Nishizawa et al. proposed broadband SPC by using comb-profile fiber (CPF) [13], where the spectra can be compressed more than 20 times in the wavelength range of 1620 to 1850 nm. In 2014, Chen, et al. numerically investigated the SPC in a comb-like distributed fiber [14], where the SPC ratio can be up to 56.23 with low pedestals. In 2016, Nishizawa et al. demonstrated an improved CPF and achieved a SPC ratio of 20.5 with dramatically suppressed side lobes [15]. In the previous works, the CPF used requires multi-stage splicing between implemented fibers, and it is difficult to realize by using conventional method of fusion splicing. In addition, the SPC and wavelength shift cannot be achieved simultaneously.

Soliton self-frequency shift (SSFS) was firstly discovered in 1986 [16], [17]. Tunable light sources are subsequently developed by using the SSFS [18]-[20]. However, in SSFS, both peak power and pulse width vary during the propagation and in general do not lead the SPC [21]-[23]. In general, SPC is caused by the interaction between group-velocity dispersion (GVD) and Kerr nonlinearity. Thus, the variations of the GVD and Kerr nonlinearity are crucial. It has been theoretically and experimentally shown that the SPC can be achieved [9]-[12] by increasing the anomalous GVD or decreasing Kerr nonlinearity during the propagation in a tapered nonlinear medium. However, it becomes difficult to taper waveguides at nanoscale. Recently, the SPC was achieved in a photonic crystal waveguide designed with an ultrafast tilting dispersion [24]. But the spectral width was only reduced by 11%. With the SSFS, SPC in a PCF was reported [25], where a SPC ratio of 6.5 was achieved in the PCF designed with increasing anomalous GVD and decreasing Kerr nonlinearity. The GVD and Kerr nonlinearity can be varied as the soliton occurs to red-shift during the propagation. Thus, it is not necessary to taper the nonlinear medium to achieve the SPC of wavelength-shifting soliton. At present, the nonlinear mechanism of the SPC accompanying with wavelength shift is not clearly specified. In this paper, when pump wavelength is located at 1550 nm, we demonstrate the SPC of wavelength-shifting soliton in a chalcogenide strip waveguide (CSW), which can be designed with increasing anomalous GVD and decreasing Kerr nonlinearity to achieve large SSFS. Moreover, we apply the SPC results to all-optical quantization. Because of the large wavelength shift and remarkable SPC, An effective quantization number of 3.66-bit can be achieved.

The paper is organized as following. In Section II, both the SPC and SSFS are qualitatively analyzed. The dispersion of

Kerr nonlinearity and Raman spectrum for three kinds of chalcogenide materials are calculated. In Section III, a strip waveguide based on Ge$_{11.5}$As$_{24}$Se$_{64.5}$ is designed. In Section IV, we use a generalized nonlinear Schrödinger equation (GNLSE) to model the nonlinear dynamics in the proposed waveguides. In Section V, the application of SPC with wavelength shift in all-optical quantization is demonstrated. In Section VI, we draw the conclusions.

2. Theoretical analysis

2.1. Qualitative analysis of the SPC and SSFS

The interaction between the GVD and Kerr nonlinearity can be modeled by the nonlinear Schrödinger equation. Following the procedure in Ref. [26], the initial evolution of instantaneous frequency $\delta\omega$ in anomalous GVD region can be approximately obtained. When the input pulse is hyperbolic secant described by $u(0, t) = A_0\mathrm{sech}(t/t_0)$, $\delta\omega (z, t)$ is derived as

$$\delta\omega\left(z,t\right) \approx -\frac{2\beta_2 z}{t_0^3}\left(N^2 - 1\right)\tanh\left(t/t_0\right)\mathrm{sech}^2\left(t/t_0\right),\tag{1}$$

where N is the soliton order defined as $N^2 = L_D/L_{NL}$, where $L_D = t_0^2/|\beta_2|$ is the dispersion length and $L_{NL} = 1/(\gamma_0 P_0)$ is the nonlinear length. $P_0 = A_0^2$ is the peak power and γ_0 is the Kerr nonlinear coefficient. The chirp C can be obtained from Eq. (1) as

$$C = \frac{\partial\delta\omega\left(z,t\right)}{\partial t} \approx -\frac{16\beta_2 z}{t_0^4}\left(N^2 - 1\right)\frac{4 - \left(e^{2t/t_0} + e^{-2t/t_0}\right)}{\left(e^{t/t_0} + e^{-t/t_0}\right)^4}.\tag{2}$$

It can be seen that C varies nonlinearly with t. The SPC can be understood from the sign of C at $t = 0$ [9]. When C is negative, both the low and high frequency components shift towards the center frequency, and SPC occurs [12], [26]. In contrast to negative C, the low and high frequency components shift towards both sides. SPC could happen for negative C [9]. Negative C requires $N < 1$ at $t = 0$ according to Eq. (2). Since $N \propto \gamma_0/|\beta_2|$ for given t_0 and A_0, increasing $|\beta_2|$ or decreasing γ_0 may lead to $N < 1$. The increments of central wavelength λ_0 and effective mode area A_{eff} lead to the decrease of γ_0. In addition, γ_0 could also be reduced if n_2 decreases with respect to the wavelength.

We then consider the Raman effect. The central frequency $\tilde{\omega}$ of the fundamental soliton is red-shifted with the rate of [17]-[19]

$$\frac{d\tilde{\omega}}{dz} = -\frac{|\beta_2(\tilde{\omega})|}{T^3(\tilde{\omega})}\frac{f_R}{1 - f_R}R[T(\tilde{\omega})],\tag{3}$$

where $T(\tilde{\omega})$ is the pulse width when soliton is located at frequency $\tilde{\omega}$, $\beta_2(\tilde{\omega})$ is the GVD coefficient at frequency $\tilde{\omega}$ and f_R is the contribution of delayed Raman response. $R[T(\tilde{\omega})]$ is a dimensionless spectral response function depending on the Raman gain spectrum g_R. Although large n_2 corresponds to strong Raman effect which is beneficial for SSFS, SSFS could be decelerated by self-steepening [27] for rapidly changing n_2 with respect to wavelength. The physical mechanism is that the molecules or phonons vibrating inelastically scatter a frequency of ω_s in the process of Raman scattering and the residual frequency is $\omega_r = \omega_p - \omega_s$, where ω_p is pump frequency. It causes the photon number is conversed while the pulse energy is loss. As a result, the SSFS is quickly suppressed because the energy becomes weak. We deduce that strong Raman effect, large n_2, and moderate decreasing rate of n_2 along wavelength makes for the SPC and wavelength shift. Recently, chalcogenide materials are found to be good candidates for the SSFS due to their large Raman gain [28], [29]. In fact, g_R of As$_2$Se$_3$ is ~780 times larger than the silica around 1550 nm [28]. Moreover, chalcogenide photonic device provides a monolithic approach to realize flexible, integrated high-index-contrast substrate [30]. Thus, we will discuss the n_2 and Raman spectrum of chalcogenide materials in the following sections.

2.2. Dispersion of Kerr Nonlinear Coefficient and Raman Spectrum Calculation

The complex Kerr nonlinear coefficient includes instantaneous nonlinear polarization of electronics and intrinsic photon absorption for most nonlinear materials. β_{TPA} represents the two-photon absorption (TPA) and is given by [31]

$$\beta_{TPA} \propto F\left(2\eta\right)\big/\left(n_0^2 E_g^3\right),\tag{4}$$

where $\eta = hc/\lambda/E_g$, h is the Planck constant, c is the light speed in a vacuum, and E_g is the bandgap energy. F depends on the band structure and describes the variation of β_{TPA} below half E_g. n_2 of the chalcogenide glass can be obtained which is proportional to G as [28], [32]

$$n_2\left(\frac{hc}{\lambda}\right) \propto \left(n_0^2 + 2\right)^3\left(n_0^2 - 1\right)\left(\frac{d}{n_0 E_s}\right)^2 G\left(\eta\right),\tag{5}$$

where n_0 is the linear refractive index, d is the mean cation-anion bond length of the bonds that are primarily responsible for the nonlinear response. $d \sim 0.25$ nm for the chalcogenide glass [33]. E_s is the Sellmeier gap with relation of $E_s = 2.5E_g$. G is calculated by the Kramas-Kronig transformation of F. The dispersion of n_2 and β_{TPA} can be calculated from Eqs. (4) and (5) if n_0 and E_g are known. Here we calculate the n_2 and β_{TPA} of As$_2$S$_3$, Ge$_{11.5}$As$_{24}$Se$_{64.5}$ and As$_2$Se$_3$ for comparison because they are often used to constitute different photonic devices [18], [29], [34]. The dispersion of n_0 expressed by Sellmeier equation for the three materials can be found in Refs. [35], [36] and the bandgap energy of As$_2$S$_3$, Ge$_{11.5}$As$_{24}$Se$_{64.5}$ and As$_2$Se$_3$ are 2.4 eV [28], 1.84 eV [37] and 1.78 eV [28], respectively.

The calculation results are normalized and illustrated in Fig. 1(a). We can see that n_2 first increases and then decreases as wavelength for the three materials. The different positions of peak values in the three curves suggest that n_2 gradually shifts towards longer wavelength as bandgap energy decreases. The n_2 of As$_2$Se$_3$ has the largest slope, which is more suitable for SPC. However, significant influence of TPA on Raman gain is observed in As$_2$Se$_3$ at 1550 nm [38], [39]. As shown in Fig. 1(a), the zero-TPA wavelength of Ge$_{11.5}$As$_{24}$Se$_{64.5}$ is reduced to 1350 nm, but the absorption tail causes small absorption of 9.3×10^{-14} cm^2/W at 1550 nm [34], which has little influence on the nonlinear applications [36]. For the As$_2$Se$_3$, n_2 slope of As$_2$S$_3$ is much smaller than those of Ge$_{11.5}$As$_{24}$Se$_{64.5}$ and As$_2$Se$_3$, which does not make for SPC. In addition, As$_2$S$_3$ has lower linear refractive index than Ge$_{11.5}$As$_{24}$Se$_{64.5}$ (2.43 to 2.66 at 1550 nm), leading a weaker confinement of optical field. And n_2 of As$_2$S$_3$ is smaller than Ge$_{11.5}$As$_{24}$Se$_{64.5}$ at wavelength of 1500 nm. Therefore, we choose Ge$_{11.5}$As$_{24}$Se$_{64.5}$ as the material for the SPC. We note that the response function $h_R(t)$ of Ge$_{11.5}$As$_{24}$Se$_{64.5}$ used in Ref. [36] does not include the Boson peak (BP) because the parameters τ_1 and τ_2 are not correctly chosen. The BP is related to the vibrations of amorphous structure and observed in most of glass materials [40]. To exactly reproduce the experimental curve of g_R including BP, we construct a new form of $h_R(t)$ as

$$h_R(t) = h_{R1}(t) + h_{R2}(t) + h_{R3}(t), \tag{6}$$

where $h_{R1}(t)$, $h_{R2}(t)$, and $h_{R3}(t)$ are the three independent functions. Their expressions are as following

$$\begin{cases} h_{R1}(t) = f_a \left(1/\tau_1^2 + 1/\tau_2^2 \right) \tau_1 \exp\left(-t/\tau_2 \right) \sin\left(t/\tau_1 \right), \\ h_{R2}(t) = f_b \left(8\tau_3 - t \right)/\tau_3^2 \exp\left(-t/\tau_3 \right), \\ h_{R3}(t) = -f_c \left(1/\tau_4^2 + 1/\tau_5^2 \right) \tau_1 \exp\left(-t/\tau_5 \right) \sin\left(t/\tau_4 \right). \end{cases} \tag{7}$$

where f_a, f_b, f_c, and τ_1 to τ_5 are the undetermined parameters which are crucial to the profile of g_R. It is found that when these
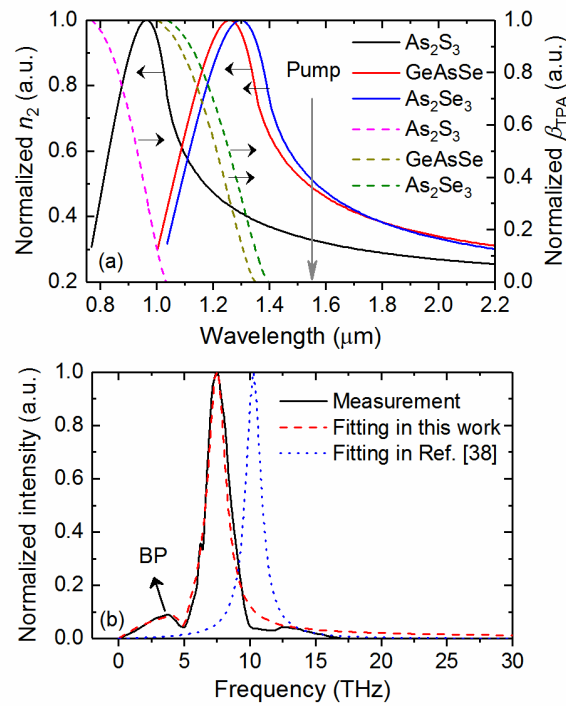

Fig. 1. (a) The dispersion of n_2 and β_{TPA} for As$_2$S$_3$ (black solid and pink dashed curves), GeAsSe (red solid and dark yellow dashed curves) and As$_2$Se$_3$ (blue solid and olive dashed curves), the gray arrow indicates the pump wavelength. (b) The extracted Raman gain spectrum of experiment (black solid curve), reproduced Raman gain spectrum from Eq. (7) (red dashed curve) and $h_R(t)$ in Ref. [36] (blue dot curve), the black arrow indicates the BP position.

parameters are chosen as listed in Table I, the BP of Ge$_{11.5}$As$_{24}$Se$_{64.5}$ can be well reproduced. Note that τ_1 to τ_5 are in fs units. Fig. 1(b) shows the experimental g_R extracted from Ref. [30], the reproduced g_R and the reported g_R in Ref. [36], respectively. The dispersion curve of reproduced g_R agrees well with the experimental one. In contrast, the reported Raman gain spectrum in Ref. [36] is very different from the experimental one because the peak value is located at longer wavelength. Therefore, we use Eq. (7) to describe the Raman effect in the following simulation.

TABLE I

PARAMETERS OF $h_R(t)$.

Parameters	f_a	f_b	f_c	τ_1 (fs)	τ_2 (fs)	τ_3 (fs)	τ_4 (fs)	τ_5 (fs)
Values	0.88	0.06	0.06	21.3	195	50	32	400

3. Waveguide design and characteristics

$Ge_{11.5}As_{24}Se_{64.5}$ waveguides can be fabricated by using thermal evaporation, photolithography, and ICP plasma etching method. The cross-section of waveguide engineered for anomalous GVD is larger than silicon since the material dispersion of $Ge_{11.5}As_{24}Se_{64.5}$ is smaller than silicon. Larger waveguide size is usually good for fiber taper coupling. Here, a bent CSW is proposed because the SSFS is proportional to the propagation distance, as indicated by Eq. (3). To enhance the ability of engineering GVD, large refractive index contrast is achieved by using the air as upper cladding, as shown in Fig. 2(b).
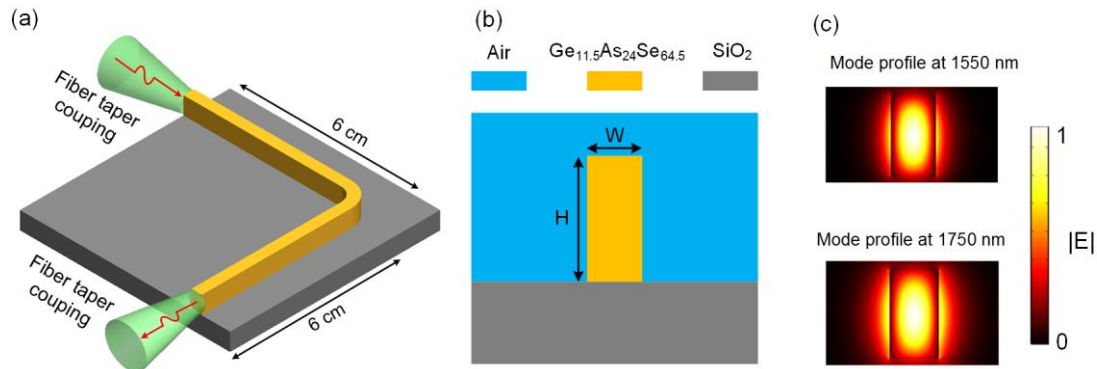

Fig. 2. (a) The three-dimensional view and (b) cross-section of the proposed CSW. (c) Optical mode profiles of quasi-TE mode calculated at wavelengths1550 and 1750 nm, respectively. The fiber taper coupling is also shown in (a).

Fig. 2(c) shows the optical mode profiles of quasi-TE mode at wavelengths 1550 and 1750 nm, respectively. When the waveguide height (H) and width (W) are chosen as 880 nm × 500 nm, the electric fields are well confined in the core region of the proposed CSW at 1550 and 1750 nm. However, in order to obtain the optimal waveguide dimension for the SSFS and SPC, we investigate β_2, β_3, E_N and γ_0 by finite element method at different H and W, as shown in Fig. 3. The confinement factor E_N is introduced to measure the energy confinement since the leakage loss becomes important at long wavelength during SSFS. E_N is defined as the ratio of energy in the core region and whole cross-section of the CSW. It is calculated by the integral of Poynting vector over the transverse. From Eq. (3), large $|\beta_2|$ is beneficial for the SSFS. $|\beta_2|$ between W ranging from 450 to 500 nm is larger than that at other areas, as indicated by the dark blue in Fig. 3(a). Moreover, when W is changed from 450 to 500 nm, β_3 is near zero, as shown in Fig. 3(b). Small β_3 can avoid the adverse effects of pulse asymmetry on the SSFS and SPC. E_N increases from 0.9 to 0.95 when W changes from 450 to 500 nm in Fig. 3(c). Such large E_N values mean that the leakage loss of the waveguide varying in this width range is relatively small. Besides, γ_0 is reduced when both W and H become large, as shown in Fig. 3(d). This is because as W and H increase, A_{eff} also increases. When H is changed from 850 to 900 nm, it is found that γ_0 has a considerable value of ~85 $W^{-1}m^{-1}$. The further calculations indicate that the SSFS can be easily triggered by using this value. Therefore, W and H are chosen in the ranges of 450 to 500 nm and 850 to 900 nm, respectively, which are illustrated by the white dashed squares in Figs. 3(a) and 3(c).
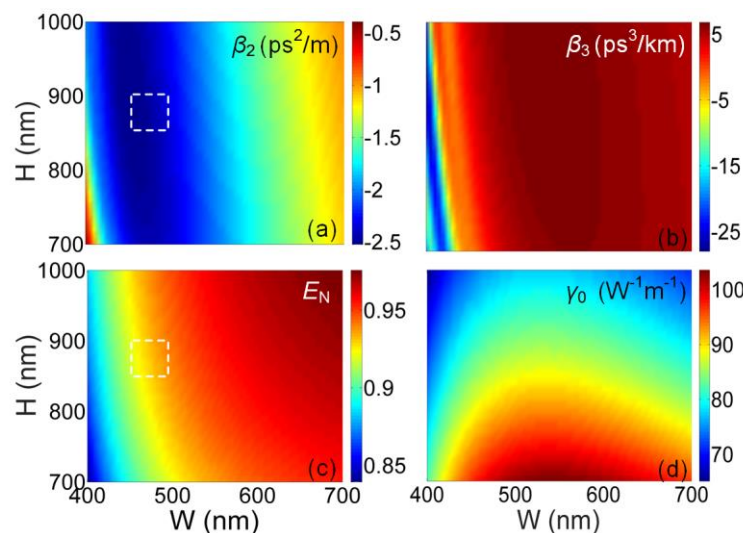

Fig. 3. Cross-sectional distribution profiles of (a) β_2, (b) β_3, (c) normalized energy E_N, and (d) γ_0 with respect to H and W at wavelength 1550 nm. The H and W are changed from 700 to 1000 nm and 400 to 700 nm, respectively. The white squares indicate the chosen regions for W and H.

To further specify H and W, we choose six combinations of $H \times W$ = 900 nm × 480 nm, 880 nm × 480 nm, 860 nm × 480 nm, 900 nm × 500 nm, 880 nm × 500 nm, and 860 nm × 500 nm. Figs. 4(a) and 4(b) show the corresponding variations of β_2, E_N, and γ_0 with wavelength. Curves of β_2 can be classified into two groups at long wavelength according to W of 480 nm and 500 nm, as shown in Fig. 4(a). We deduce that W plays a more important role in determining β_2 at longer wavelength than H. When W = 500 nm, the value of $|\beta_2|$ is larger than that of W = 480 nm, and both the SPC and SSFS may occur easily. The

similar behavior is also seen from the curves of E_N. Hence, $W = 500$ nm is preferred in the waveguide design. A moderate
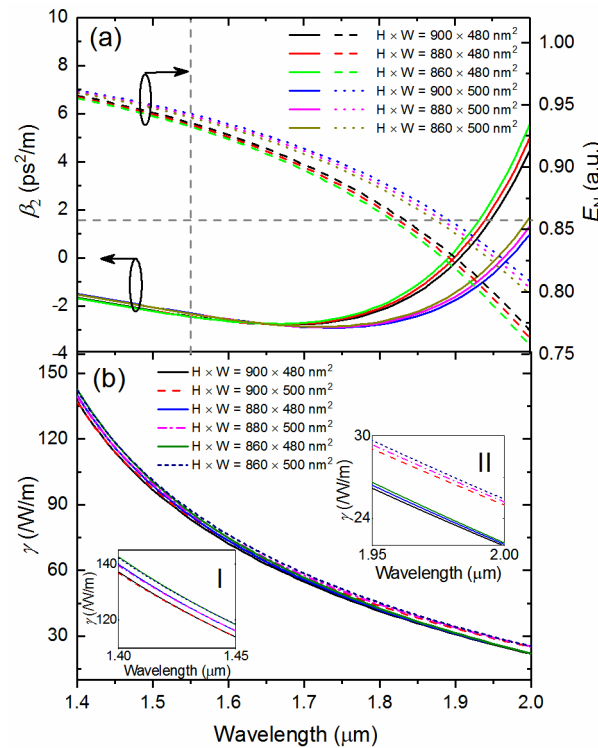

Fig. 4. (a) The variation of β_2 (solid curves) and E_N (dashed curves) with respect to the wavelength. Solid and dashed curves with the same color represent the same dimension of $H \times W$ for β_2 and E_N, respectively. (b) The variation of γ as a function of wavelength for the six different dimensions. Insets I and II show the details of γ_0 in the wavelength range of 1.4 to 1.45 μm and 1.95 to 2 μm, respectively.

H of 880 nm is chosen, and differences are very small when $H = 900$, 880, and 860 nm, respectively. Fig. 4(b) shows the variation of γ_0 with wavelength. It can be seen that γ_0 decreases monotonically along the wavelength for all combinations and the difference between six curves is very small. However, detailed observation suggests that the six curves can be divided into three groups according to different H at short wavelength and two groups according to different W at long wavelength, as shown in insets I and II of Fig. 4(b), respectively. These results indicate that H plays a more important role than W at short wavelength in determining γ_0. Oppositely, W is more crucial than H at long wavelength in determining γ_0.

4. Simulation results and discussion

The nonlinear dynamics of optical pulse propagation in the proposed CSW can be modeled by the GNLSE as

$$\frac{\partial u}{\partial z} + \frac{\alpha}{2} u + \sum_{m=2}^{12} \frac{i^{m-1} \beta_m}{m!} \frac{\partial^m u}{\partial t^m} = i \left(\frac{i \beta_{TPA}}{2 A_{eff}} + \sum_{n=0}^{6} \frac{\gamma_n}{n!} \frac{i^n \partial^n}{\partial t^n} \right) \times u \int_0^\infty R_1(t') \left| u(z, t-t') \right|^2 dt',$$ (8)

where $\alpha = 0.6$ dB/cm is the linear loss [34], $\beta_m = d^m \beta/d\omega^m$ is the m-th order dispersion coefficient of the propagation constant β, β_{TPA}/A_{eff} describes the wavelength-dependent TPA, $\gamma_n = d^n \gamma_0/d\omega^n$ is the n-th order dispersion coefficient of Kerr nonlinearity, and $R_1(t')$ is the nonlinear response function written as

$$R_1(t') = (1 - f_R) \delta(t') + f_R h_R(t').$$ (9)

The value of f_R is 0.13 [41], and the form of $h_R(t')$ is given in Eq. (7). The dependence of α on the wavelength is neglected in our model due to its small variation with wavelength. It should be noted that the number of photons but not the energy is conserved because of Raman scattering when the shock-wave term $\gamma_n/n!(i^n \partial^n/\partial t^n)$ is included.

An initial optical pulse with the form of $u(z,t) = A_0 \mathrm{sech}(t/t_0)$ is injected into the proposed CSW, where t_0 is the pulse width. The input pulse has a full width at half maximum (FWHM) T_{FWHM} of 50 fs where $T_{FWHM} \approx 1.763\, t_0$ for hyperbolic secant pulse. The input peak powers of 25 and 75 W are chosen for comparison. The spectral and temporal evolutions along the propagation distance z are shown in Fig. 5. The top panels are the output waveforms and bottom panels are the pulse evolutions. It can be seen from Figs. 5(a) and 5(b) that both spectra are significantly compressed at the end of propagation. However, the spectrum is not only compressed but also evidently red-shifted when input peak $P_0 = 75$ W. for $P_0 = 25$ W, small wavelength shift is observed shown in Fig. 5(b). Correspondingly, the temporal delay under $P_0 = 25$ W is much less than that of 75 W (5 ps versus 40 ps), as shown in Figs. 5(c) and 5(d). In the process of SSFS, soliton radiation can be observed during the propagation. The travelling pulse adjusts its temporal profile to maintain the soliton order N. However, the SPC of wavelength-shifting soliton can be achieved in our proposed CSW. Significant spectral fluctuations before 6 cm can be seen in Fig. 5(a). This is the natural results when pulse evolves to the fundamental soliton. The spectral fluctuation should be
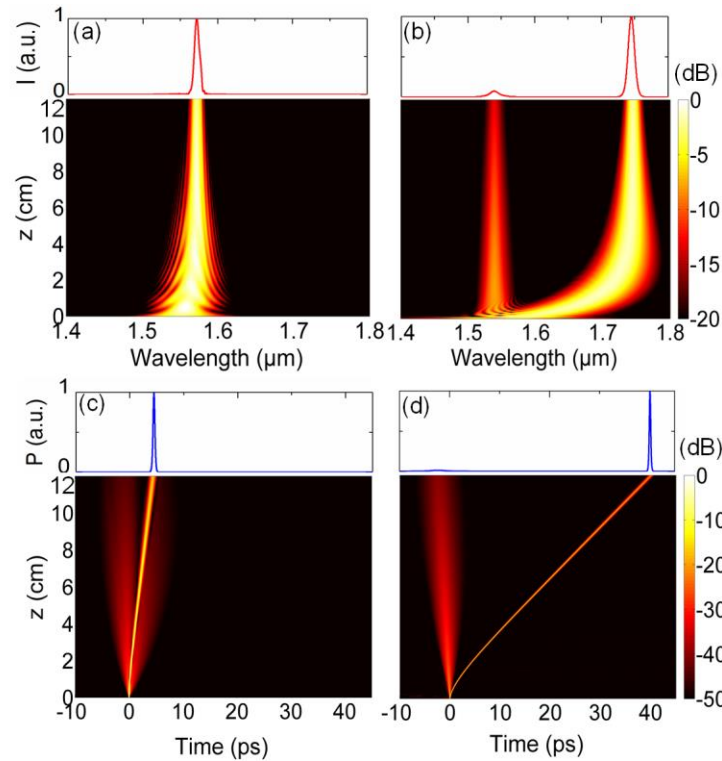
Fig. 5. The output spectra (top panel) and evolutions of the spectra along propagation distance z (bottom panel) are shown in (a) P_0=25 W and (b) P_0=75W. (c) Output temporal pulse (top panel) and evolution of temporal pulse along z (bottom panel) are shown in (c) P_0= 25 W and (d) P_0=75 W.

stronger for P_0= 75 W. However, we cannot clearly see that in Fig. 5(b). This is because the nonlinear process occurs too fast for the higher P_0. Instead, the interference between the residual pump and red-shifted soliton can be clearly observed before the pulse is shifted to longer wavelength in Fig. 5(b). The higher P_0 leads higher residual pump, which sustains over the whole propagation. From the point of chirp, the corresponding soliton order is 0.87 when P_0 = 25 W. In this case, GVD plays a more important role than Kerr nonlinearity and C is negative. As a result, the leading/trailing edges move towards the lower/higher frequency and SPC occurs. The N becomes ~1.49 when P_0 =75 W. Kerr nonlinearity plays a dominate role and C is positive. Therefore, spectral broadening may be seen at the initial stage of the propagation. However, the case is changed after the input pulse is red-shifted to longer wavelength. On one hand, γ_0 rapidly decreases because of the combined action of decreasing n_2, increasing λ_0 and A_{eff}. On the other hand, $|\beta_2|$ increases along the propagation. As a result, $N < 1$ may occur because $L_D < L_{NL}$. Negative C is formed and SPC occurs in this process.

Fig. 6(a) shows the variation of central wavelength λ_0 with respect to z for P_0 = 25, 35, 45, 55, 65, and 75 W, respectively. We can see that λ_0 firstly increases and then almost keeps unchanged along the propagation for all P_0. Larger P_0 corresponds to faster growth of λ_0 before it reaches the maximum. Such "saturation" of wavelength shift is due to the decrease of peak power during the propagation. Wavelength shift will not be triggered when peak power is too low. Fig. 6(b) shows the corresponding variations of spectral width. It can be seen that the SPC occurs during the whole propagation. However, spectral broadening caused by the SPM could perturb the SPC at the initial stage if P_0 is very high, e.g. P_0 = 75 W. Detailed observation shows that input optical spectrum quickly expands from 52.04 to 121.8 nm at the propagation distance of 0.072 cm. Spectral broadening can hardly be seen when P_0 =25 W. In fact, the optical spectrum is directly narrowed from 52.04 to 7.23 nm. However, while lower P_0 makes for SPC, the wavelength shift occurs slowly. A wavelength shift of only 17 nm can be obtained at the end of propagation. But significant wavelength shift of 190 nm can be observed when P_0 = 75 W. It should be noted that small fluctuations in the curves for all P_0 can be seen from Figs. 6(a) and 6(b). This is because the spectral waveform is very sensitive to the nonlinear interaction, which results in rapid variations of λ_0 and λ_{FWHM} during the propagation. However, the SPC of wavelength-shifting soliton under the considered P_0 can be achieved. The output waveforms can maintain their profiles very well during the processes of SPC and SSFS, as shown in Fig. 6(c).
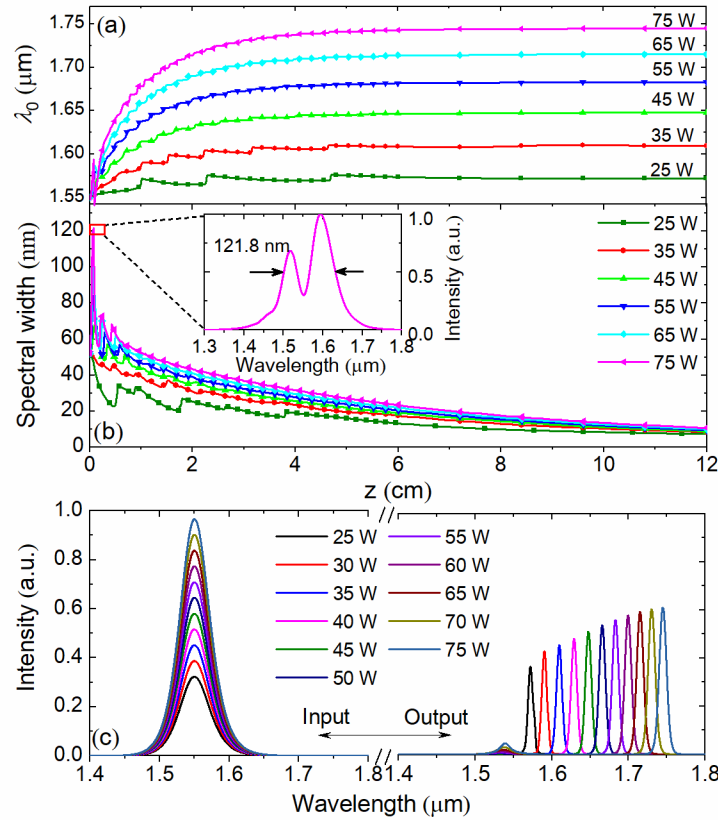
Fig. 6. (a) The variations of central wavelength and (b) spectral width with respect to z for different P_0. The pink, cyan, blue, green, red and olive solid curves represent P_0 = 75, 65, 55, 45, 35, and 25 W, respectively. The inset is the spectral for the first high peak of spectral width when P_0 = 75 W.

In order to study the dynamics of the SPC and SSFS, the variation of N is investigated during the propagation. In Fig. 7(a), N gradually approaches to 1 when the initial N values are 0.87 and 1.49 respectively. This phenomenon suggests that input pulse can gradually form the fundamental soliton during the process of SPC and SSFS if the initial N satisfies the condition $0.5 < N < 1.5$. However, the evolution details are different for the two cases. For P_0 = 25 W, the oscillation of N is weak and slow. But it becomes strong and fast, and then quickly disappears when P_0 = 75 W. Spectral compression factor (SCF) and brightness-enhanced factor (BEF) are introduced to further characterize the SPC. The SCF is defined as the ratio of input and output spectral FWHM, and BEF is defined as the ratio of output and input spectral peak intensity. In Fig. 7(b), the SCF under P_0 = 25 W is 7.2 while the SCF under P_0 = 75 W is only 4.9 at the end of propagation. In addition, in Fig. 7(c), the corresponding BEF under P_0 = 25 W is also larger than that under P_0 = 75 W over the whole propagation (1.13 versus 0.63). The SCF, BEF, and amount of wavelength shift are determined by P_0. This finding inspires us to apply the SPC of wavelength-shifting soliton to the all-optical quantization. Thus, we conclude that low P_0 has advantage both in SCF and BEF. However, this advantage is at the expense of wavelength shift. The amount of wavelength shift under P_0 = 25 W is ten times smaller than that under P_0 = 75 W. This remarkable difference indicates that tunable SPC accompanying with broadband wavelength shift under higher P_0 maybe more functional in some applications where SCF and BEF are not strongly required.
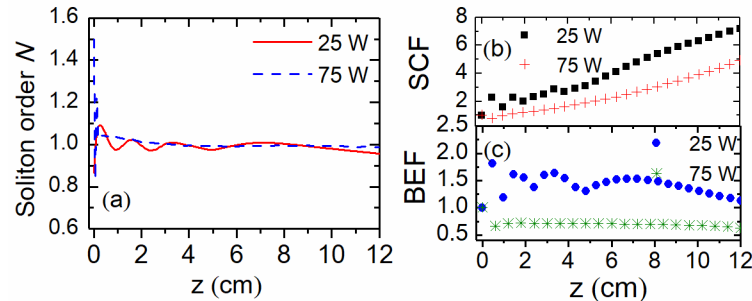

Fig. 7. (a) The variation of soliton order N as a function of z for P_0 =25 W (red solid curve) and 75 W (blue dashed curve). (b) SCF as a function of z for P_0 = 25 W (black square) and 75 W (red plus sign). (c) BEF as a function of z for P_0 = 25 W (blue solid circle) and 75 W (olive snow symbol).

5. The application in integratable all-optical quantization

5.1. Principle of all-optical quantization

The schematic diagram of the proposed all-optical quantization based on the SPC of soliton is shown in Fig. 8. The input analog-sampled signals with different powers are launched into the CSW. Each sampled signal experiences SPC and SSFS. The sampled pulse with specific peak power can be identified referring to a specific central wavelength since the amount of

wavelength shift is directly proportional to P_0. The CSW is then followed by a proper de-multiplexer for wavelength de-multiplexing. The identified signals with different P_0 at specific ports are filtered out. The quantization resolution M of this scheme can be given by [4]

$$M = \log_2 \left(\frac{\lambda_{\text{shift}} + \lambda_{\text{FWHM}}}{\lambda_{\text{FWHM}}} \right),$$ (10)

where λ_{shift} is the amount of wavelength shift and λ_{FWHM} is the FWHM of output optical spectrum. It is evident that M is directly proportional to λ_{shift} and inversely proportional to λ_{FWHM}, respectively.
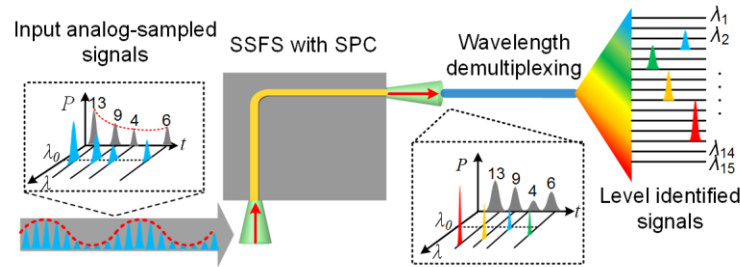

Fig. 8. Schematic diagram of the proposed all-optical quantization based on the SPC of soliton in the designed CSW.

5.2. Results of all-optical quantization

After the signal pulses are quantified, optical interconnection coding based on the binary code conversion are employed to obtain the Gray codes, as shown in Ref. [4]. In the scheme of all-optical quantization, the maximum P_0 of signal pulse is set as 64 W, corresponding to N =1.39. The minimum P_0 is 25 W for wavelength shift. In order to obtain the positions of central wavelength of 15 filtering windows, P_0 of 15 input signal pulses are set in Table II.

TABLE II
PEAK POWERS (P_0) OF DIFFERENT FILTERING WINDOWS.

No.	1	2	3	4	5	6	7	8
P_0 (W)	25	27.8	30.5	33.1	35.7	38.2	40.8	43.5
No.	9	10	11	12	13	14	15	
P_0 (W)	46.2	49	51.8	54.7	57.8	60.8	64	

For the 15 input signal pulses, the corresponding output spectra after SPC and wavelength shift are shown in Fig. 9(a). Each spectrum profile shows a single peak without overlap to the adjacent one. The power levels of input signal pulses can be identified referring to different central wavelengths. Thus, specific level identified signal at a specific port can be obtained.

TABLE III
CENTRAL WAVELENGTH AND BANDWIDTHS OF CHOSEN FILTERS.

Central wavelengths of filters (nm)	Bandwidths of filters (nm)	Central wavelengths of filters (nm)	Bandwidths of filters (nm)
1572	7.2	1652	6.4
1582	7.2	1662	6.4
1592	6.8	1672	6.4
1602	6.8	1682	6.4
1612	6.6	1692	6.3
1622	6.6	1702	6.3
1632	6.5	1712	6.4
1642	6.5		

Accordingly, we set 15 filter windows of a de-multiplexer ranging from 1572 to 1712 nm with the same wavelength interval of

10 nm, as shown in Table III. Rational allocation of filters can lower the quantization error induced by non-uniform spectral width during the process of SSFS. The power transfer functions of four output ports b1-b4 after filtering are shown in Fig.
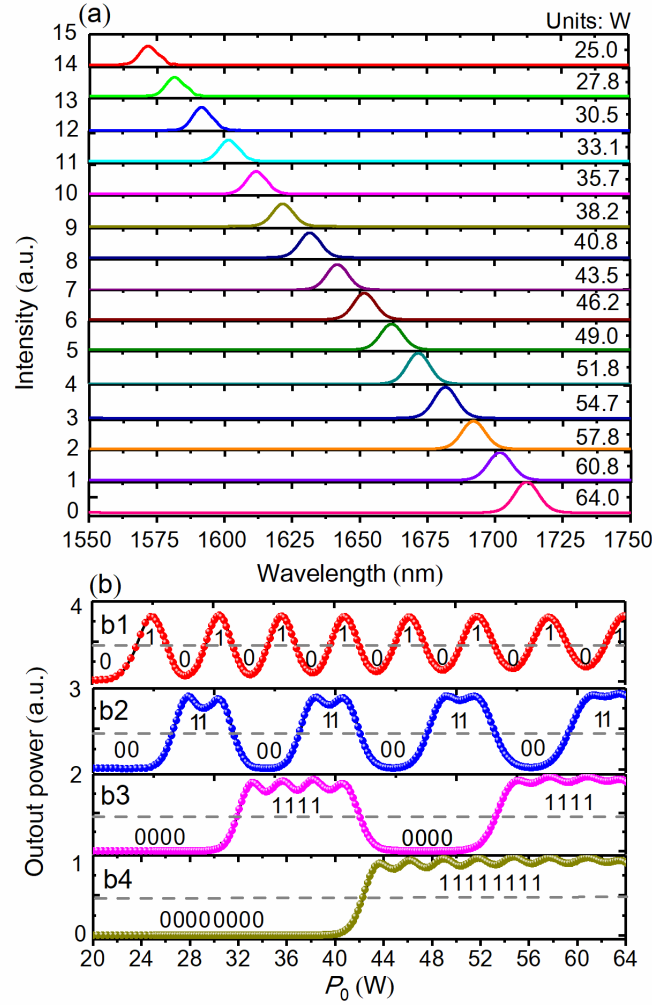

Fig. 9. (a) Output spectral intensity of quantized pulses under different P_0 = 25, 27.8, 30.5, 33.1, 38.2, 40.8, 43.5, 46.2, 49, 51.8, 54.7, 57.8, and 64 W. (b) The power transfer functions of the four output ports, b1, b2, b3, and b4.

9(b). We can obtain the binary codes with proper decision threshold. Quantization error would be introduced if the threshold transition points of the four power transfer functions were not perfectly aligned. As a result, M will be degraded. The effective number of bit (ENOB) of all-optical quantization is defined as [4]

$$\text{ENOB} = \frac{20\log\left(P_S/P_N\right)}{6.02},\tag{11}$$

where P_S and P_N are the powers of signal and noise root mean-square without the DC component, respectively. P_S and P_N are given by [42]

$$P_S = \frac{P_{FS}}{\sqrt{12}},\tag{12a}\qquad\qquad P_N \approx \sqrt{\frac{1}{12}\left(\frac{P_{FS}}{2^M}\right)^2 + \frac{1}{2^M}\sum_{i=0}^{15}\left(\Delta P_{stepi}\right)^2},\tag{12b}$$

where P_{FS} is the full-scale of output power range, ΔP_{stepi} is the error, indicating the power difference between the ideal case and simulation result. P_{FS} is calculated as 44 W when P_0 changes from 20 to 64 W. We carefully compare the power difference between the ideal case and simulation result in order to determine ΔP_{stepi}, as shown in Fig. 10(a). ΔP_{step14} is shown in the inset of Fig. 10(a). When P_0 is chosen as 20 and 64 W, the corresponding central wavelengths are 1560 and 1712 nm, respectively, which gives a λ_{shift} of 152 nm. The maximum λ_{FWHM} is 10 nm with P_0 = 64 W. We can get an ideal quantization resolution of 4-bit according to Eq. (10). Therefore, the least significant bit (LSB) defined as LSB = PFS/2M is 2.75. An ENOB of 3.66-bit can be further obtained from Eq. (11). Only 0.34-bit difference compares with the ideal resolution of 4-bit. The differential nonlinearity (DNL) and integral nonlinearity (INL) errors, which are used to evaluate the performance of ADC, are given by [43]

$$\text{DNL}(i) = \frac{w(i) - \text{LSB}}{\text{LSB}} = \frac{P_{i+1} - P_i - \text{LSB}}{\text{LSB}},\quad 0 \leq i \leq 2^M - 1\tag{13}$$

$$\mathrm{INL}(i) = \frac{\Delta P_{stepi}}{P_{FS}} = \frac{P_{ideal}(i) - P_i}{2^N \times LSB}, \quad 0 \le i \le 2^M - 1 \tag{14}$$

where P_i and P_{ideal} are P_0 under the simulation and ideal cases, respectively, and i represents the output digital value varying from 0 to 15. We estimate the DNL and INL errors according to the quantization transfer function shown in Fig. 10(a). Fig. 10(b) shows the variations of the DNL and INL with respect to the output digital value. It can be seen that the maximum DNL is − 0.425 LSB at output digital value of 15 and the maximum INL is − 0.027 LSB at output digital value of 14, which are smaller than the error threshold of 0.5 LSB.
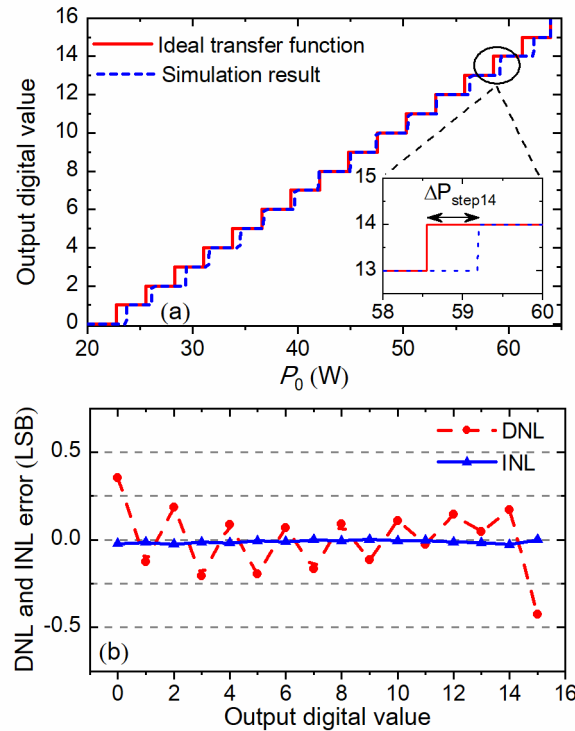

Fig. 10. (a) The quantization transfer functions of the proposed scheme, and (b) the variations of DNL and INL as functions of output digital value.

6. Conclusion

In summary, we numerically demonstrate an efficient SPC of wavelength-shifting soliton in a proposed CSW. Qualitative analysis indicates that the increasing GVD and decreasing Kerr nonlinearity along propagation direction jointly induce the SPC. Large nonlinear refractive index is necessary for the Raman gain. $Ge_{11.5}As_{24}Se_{64.5}$ is chosen as the waveguide material for the SPC and SSFS. A CSW is designed to obtain increasing anomalous GVD and decreasing Kerr nonlinearity along the wavelength. Simulation results show that SPC from 52.04 to 7.23 nm with wavelength shift of 17 nm can be realized when $P_0 = 25$ W. However, although the SPC from 52.04 to 10.64 nm is slightly weakened when $P_0 = 75$ W, the wavelength shift is enhanced up to 190 nm. The SPC of wavelength-shifting soliton is then applied to all-optical quantization. An ENOB of 3.66-bit with only 0.34-bit difference from the ideal resolution of 4-bit can be achieved. Our research results are expected to have important applications in on-chip integrated spectroscopy, all-optical signal processing, etc.

Acknowledgements

References

[1] M. Oberthaler, and R. A. Höpfel, "Special narrowing of ultrashort laser pulses by self-phase modulation in optical fibers," Applied Physics Letter, vol. 63, no. 8, pp. 1017-1019, 1993.

[2] G. C. J. Fatome, B. Kibler, E. R. Andresen, H. Rigneault, and C. Finot, "All-fiber spectral compression of picosecond pulses at telecommunication wavelength enhanced by amplitude shaping," Applied Optics, vol. 51, no. 19, pp. 4547-4553, 2012.

[3] M. Rusu, and O. G. Okhotnikov, "All-fiber picosecond laser source based on nonlinear spectral compression," Applied Physics Letter, vol. 89, pp. 091118-1-3, 2006.

[4] T. Nishitani, T. Konishi, and K. Itoh, "Resolution Improvement of All-Optical Analog-to-Digital Conversion Employing Self-frequency Shift and Self-Phase-Modulation-Induced Spectral Compression," IEEE Journal of Selected Topics in Quantum Electronics, vol. 14, no. 3, pp. 724-732, 2008.

[5] B. R. Washburn, J. A. Buck, and S. E. Ralph, "Transform-limited spectral compression due to self-phase modulation in fibers," Optics Letter, vol. 25, no. 7, pp. 445-447, 2000.

[6] E. R. Andresen, J. M. Dudley, D. Oron, C. Finot, and H. Rigneault, "Transform-limited spectral compression by self-phase modulation of amplitude-shaped pulses with negative chirp," Optics Letter, vol. 36, no. 5, pp. 707-709, 2011.

[7] E. R. Andresen, J. Thøgersen, and S. R. Keiding, "Spectral compression of femtosecond pulses in photonic crystal fibers," Optics Letter, vol. 30, no. 15, pp. 2025-2027, 2005.

[8] D. A. Sidorov-Biryukov, A. Fernandez, L. Zhu, A. Pugžlys, E. E. Serebryannikov, A. Baltuška, and A. M. Zheltikov, "Spectral narrowing of chirp-free light pulses in anomalously dispersive, highly nonlinear photonic-crystal fibers," Optics Express, vol. 16, no. 4, pp. 2502-2507, 2008.

[9] R. Liang , X. Zhou, Z. Zhang, Z. Qin, H. Li, and Y. Liu, "Numerical investigation on spectral compression of femtosecond soliton in a dispersion-increasing fiber," Optical Fiber Technology, vol. 15, pp. 438-441, 2009.

[10] H. Chuang, and C. Huang, "Wavelength-tunable spectral compression in a dispersion-increasing fiber," Optics Letter, vol. 36, no. 15, pp. 2848-2850, 2011.

[11] W. Chao, Y. Lin, J. Peng, and C. Huang, "Adiabatic pulse propagation in a dispersion-increasing fiber for spectral compression exceeding the fiber dispersion ratio limitation," Optics Letter, vol. 39, no. 4, pp. 853-856, 2014.

[12] Q. Li, T. Zhang, and M. Li, "Spectral compression of chirp-free optical pulses in fibers with exponentially increasing dispersion," Journal of Optical Society of America B, vol. 34, no. 9, pp. 1796-1804, 2017.

[13] N. Nishizawa, K. Takahashi, Y. Ozeki, and K. Itoh, "Wideband spectral compression of wavelength-tunable ultrashort soliton pulse using comb- profile fiber ," Optics Express. vol. 18, no. 11, pp. 11700-11706, 2010.

[14] Y. Chen, Z. Zhang, X. Zhou, X. Chen, Y. Liu, "Spectral compression in a comb-like distributed fiber and its application in 7-bit all-optical quantization," Optics Engineering, vol. 53, no. 12, pp. 126106-1-9, 2014.

[15] N. Nishizawa, Y. Andou, E. Omoda, H. Kataura, and Y. Sakakibara, "Characteristics and improvement of wideband wavelength-tunable narrow-linewidth source by spectral compression in quasi-dispersion- increasing comb-profile fiber," Optics Express, vol. 24, no. 20, pp. 23403-23418, 2016.

[16] F. M. Mitschke, and L. F. Mollenauer, "Discovery of the soliton self-frequency shift," Optics Letter, vol. 11, no. 10, pp. 659-661, 1986.

[17] J. P. Gordon, "Theory of the soliton self-frequency shift," Optics Letter, vol. 11, no. 10, pp. 662-664, 1986.

[18] A. M. Al-kadry, and M. Rochette, "Mid-infrared sources based on the soliton self-frequency shift," Journal of Optical Society America B, vol. 29, no. 6, pp. 1347-1355, 2012.

[19] A. Al-Kadry, and M. Rochette "Maximized Soliton Self-Frequency Shift in Non-Uniform Microwires by the Control of Third-Order Dispersion Perturbation," Journal of Lightwave Technology, Vol. 31, no. 9, pp. 1462-1467, 2013.

[20] M. Y. Koptev, E. A. Anashkina, A. V. Andrianov, V. V. Doroeev, A. F. Kosolapov, S. V. Muravyev, and A. V Kim, "Widely tunable mid-infrared fiber laser source based on soliton self-frequency shift in microstructured tellurite fiber," Optics Letter, vol. 40, no. 17, pp. 4094-4097, 2015.

[21] J. Santhanama, G. P. Agrawal, "Raman-induced spectral shifts in optical fibers: general theory based on the moment method," Optics Communication, vol. 222, pp. 413-420, 2003.

[22] N. Gonz´alez-Baquedano, I. Torres-G´omez, N. Arzate, A. Ferrando, and D. E. Ceballos-Herrera, "Pulse quality analysis on soliton pulse compression and soliton self-frequency shift in a hollow-core photonic bandgap fiber," Optics Express, vol. 21, no. 7, pp. 9132-9143, 2013.

[23] T. N. Nguyen, K. Kieu, D. Churin, T. Ota, M. Miyawaki, and N. Peyghambarian, "High Power Soliton Self-Frequency Shift with Improved Flatness Ranging from 1.6 to 1.78 µm," Photonics Technology Letter, vol. 25, no. 19, pp. 1893-1896, 2013.

[24] D. M. Beggs, T. F. Krauss, L. Kuipers, and T. Kampfrath, "Ultrafast Tilting of the Dispersion of a Photonic Crystal and Adiabatic Spectral Compression of Light Pulses," Physics Review Letter, vol. 108, pp. 033902-1-5, 2012.

[25] A. B. Fedotov, A. A. Voronin, I. V. Fedotov, A. A. Ivanov, and A. M. Zheltikov, "Spectral compression of frequency-shifting solitons in a photonic-crystal fiber," Optics Letter, vol. 34, no. 5, pp. 662-664, 2009.

[26] D. Anderson, M. Desaix, M. Karlsson, M. Lisak, and M. L. Quiroga-Teixeiro, "Wave-breaking-free pulses in nonlinear-optical fibers," Journal of Optical Society of America B, Vol. 10, no. 7, pp. 1185-1190, 1993.

[27] A. A. Voronin, and A. M. Zheltikov, "Soliton self-frequency shift decelerated by self-steepening," Optics Letter, Vol. 33, no. 15, pp. 1723-1725, 2008.

[28] R. E. Slusher, G. Lenz, J. Hodelin, J. Sanghera, L. B. Shaw, and I. D. Aggarwal, "Large Raman gain and nonlinear phase shifts in high-purity As$_2$Se$_3$ chalcogenide fibers," Journal of Optical Society of America B, vol. 21, no. 6, pp. 1146-1155, 2004.

[29] A. C. Judge, S. A. Dekker, R. Pant, C. Martijn de Sterke, and B. J. Eggleton, "Soliton self-frequency shift performance in As2S3 waveguides," Optics Express, vol. 18, no. 14, pp. 14960-14968, 2010.

[30] L. Li, H. Lin, S. Qiao, Y. Zou, S. Danto, K. Richardson, J. D. Musgraves, N. Lu, and J. Hu, "Integrated flexible chalcogenide glass photonic devices," Nature Photonics, vol. 8, pp. 643-649, 2014.

[31] E. W. Van Stryland, M. A. Woodall, H. Vanherzeele, and M. J. Soileau "Energy band-gap dependence of two-photon absorption," Optics Letter, vol. 10, no. 10, pp. 490-492, 1985.

[32] M. Sheik-Bahae, D. J. Hagan, and E. W. Van Stryland, "Dispersion and Band-Gap Scaling of the Electronic Kerr El'ect in Solids Associated with Two-Photon Absorption," Physics Review Letter, vol. 65, no. 1, pp, 96-99, 1990.

[33] G. Lenz, J. Zimmermann, T. Katsufuji, M. E. Lines, H. Y. Hwang, S. Sp¨ alter, R. E. Slusher, and S.-W. Cheong, "Large Kerr effect in bulk Se-based chalcogenide glasses," Optics Letter, vol. 25, no. 4, pp. 254-256, 2000.

[34] X. Gai, S. Madden, D. Choi, D. Bulla, and B. Luther-Davies, "Dispersion engineered Ge$_{11.5}$As$_{24}$Se$_{64.5}$ nanowires with a nonlinear parameter of 136 W^{-1}m^{-1} at 1550nm," Optics Express, Vol. 18, no. 18, pp. 18866-18874, 2010.

[35] A. B. Salem, R. Cherif, and M. Zghal, "Soliton-self compression in highly nonlinear chalcogenide photonic nanowires with ultralow pulse energy," Optics Express, vol. 19, no. 21, pp. 19955-19966, 2011.

[36] M. R. Karim, B. M. A. Rahman, and G. P. Agrawal, "Mid-infrared supercontinuum generation using dispersion-engineered Ge$_{11.5}$As$_{24}$Se$_{64.5}$ chalcogenide channel waveguide," Optics Express, vol. 23, no. 5, pp. 6903-6914, 2015.

[37] A. Prasad, C. Zha, R. Wang, A. Smith, S. Madden, and B. Luther-Davies "Properties of Ge$_x$As$_y$Se$_{1-x-y}$ glasses for all-optical signal processing," Optics Express, vol. 16, no. 4, pp. 2804-2815, 2008.

[38] A. Tuniz, G. Brawley, D. J. Moss, and B. J. Eggleton, "Two-photon absorption effects on Raman gain in single mode As$_2$Se$_3$ chalcogenide glass fiber," Optics Express, vol. 16, no. 22, pp. 18524-18534, 2008.

[39] H. Steffensen, C. Agger, and O. Bang "Influence of two-photon absorption on soliton self-frequency shift," Journal of Optical Society of America B , vol. 29, no. 3, pp. 484-492, 2012

[40] V. K. Tikhomirov, L. F. Santos, R. M. Alemida, A. Jha, J. Kobelke, and M. Scheffler, "On the origin of the Boson peak in the Raman scattering spectrum of As2S3 glass," Journal of Non-crystal Solid, Vol. 284, pp. 198-202, 2001.

[41] X. Gai, R. P. Wang, C. Xiong, M. J. Steel, B. J. Eggleton, and B. Luther-Davies, "Near-zero anomalous dispersion Ge$_{11.5}$As$_{24}$Se$_{64.5}$ glass nanowires for correlated photon pair generation: design and analysis," Optics Express, vol. 20, no. 2, pp. 776-786, 2012.

[42] S. J. Tilden, T. E. Linnenbrink, and P. J. Green, "Overview of IEEE-STD-1241" standard for terminology and test methods for analog-to-digital converters," in Instrumentation and Measurement Technology Conference, IMTC/99. Proceedings of the 16th IEEE. IEEE, vol. 3, 1999, pp: 1498-1503.

[43] S. J. Tilden, T. E. Linnenbrink, and P. J. Green. "Standard for terminology and test methods for analog-to-digital converters: a case study of utilization of IEEE-STD-1241." Computer Standards & Interfaces, vol. 22, no. 2, pp. 103-112, 2000.